

Very-Long-Wavelength Quantum Well Infrared Photodetector

Meimei Z. Tidrow^a, Xudong Jiang^b, Jung-Hee Lee^b, Sheng S. Li^b, Junhee Moon^b, W. K. Liu^c and K. Bacher^c

^aU.S. Army Research Laboratory, Adelphi, MD 20783-1197

^bUniversity of Florida, Gainesville, FL 32611

^cQuantum Epitaxial Designs, Inc., Bethlehem, PA 18015

ABSTRACT

Infrared detector is a very important part of infrared sensor technology. In ballistic missile defense, infrared sensors play an important role in missile seeking, tracking, guiding, discriminating, and intercepting. Tactical applications for endo-atmospheric situation are mostly under a high background (300K), where a high operating temperature above liquid nitrogen (77K) is desired. IR materials such as HgCdTe, InSb, PtSi and quantum well infrared photodetectors (QWIP) are all suitable detector material systems for tactical applications, in which some material systems are more mature than others. For strategic applications, such as exo-atmospheric interceptors and space-based surveillance sensors, the target is usually far away with a cooler temperature, under a cold background. The detection wavelength of the detector under this situation needs to be at very-long-wavelength region ($>12\ \mu\text{m}$) for efficient detection of the cool target. The current state of the art HgCdTe (MCT) based IR detectors have not met all these requirements, and QWIPs provide a useful alternative for VLWIR applications. In this presentation, an overview of VLWIR QWIPs is given and three detailed detector structures and performance are discussed.

1. INTRODUCTION

Infrared (IR) detection has been extensively investigated since the discovery of IR radiation in 1800. The IR spectrum can be divided into short wave IR (SWIR) (1 to 3 μm), medium wave IR (MWIR) (3 to 5 μm), long wave IR (LWIR) (8 to 12 μm), and very long wave IR (VLWIR) ($>12\ \mu\text{m}$). IR focal plane array (FPA) technology is very important to ballistic missile defense, such as missile guidance, tracking, and

interception. IR detection has vast military and commercial applications. The military applications could include night vision, rifle sight, surveillance, and target acquisition and discrimination. Commercial applications of IR FPA could cover medical, fire control, surveillance and driver's vision enhancement. For ballistic missile defense, endoatmospheric interceptors and airborne surveillance sensors used for tactical applications typically observe warm targets with high background irradiance from heated windows, scattered sunlight, and the earth's surface. The IR detector wavelength for endoatmospheric situation is required to be within the atmospheric transmission windows, saying 3 to 5 μm and 8 to 12 μm . In contrast, exoatmospheric interceptors and space based surveillance sensors used for strategic applications typically engage cool targets with low background irradiance levels. The targets are often far away and unresolved at the early stage of detection. LWIR, and especially VLWIR are needed wavelength bands. In order to eliminate the earth shine, the detectors should be designed to avoid the atmospheric transmission windows.

Intersubband transitions in III-V semiconductor heterostructures have been widely investigated for quantum well infrared photodetectors (QWIPs) applications [1]. Due to its material growth maturity, large array uniformity and detection wavelength flexibility, high performance and large format (640 \times 480) GaAs/AlGaAs QWIP focal plane arrays (FPAs) have been successfully demonstrated, which challenge other infrared detector systems such as HgCdTe, PtSi, InSb, and Si:Ge for the mid-wavelength infrared (MWIR) and long-wavelength infrared (LWIR) detection. Most of the QWIP research works have been focused on the spectral regions of MWIR (3-5 μm) and LWIR (8-12 μm) bands during the past decade. Various QWIP structures have been developed to meet different application requirements. In addition, several light-coupling and grating techniques have been developed to increase the absorption quantum efficiency of QWIPs in the mid- and long- wavelength infrared atmospheric spectral windows [2, 3].

In this paper, we will emphasize on the VLWIR detectors. The VLWIR detectors are of great interest for many applications such as measuring vertical temperature profiles of the atmosphere, studying the composition, structure, and the energy balance of molecular clouds and stars. It is especially important in strategic and

space applications to detect far away targets with a cold background. These applications have placed stringent requirements on the performance of IR detectors and arrays such as high detectivity, low dark current, high uniformity, radiation hardness, and low power dissipation. The current state of the art HgCdTe (MCT) based IR detectors have not met all these requirements, and QWIPs provide a useful alternative for VLWIR applications.

Recent works on the VLWIR QWIPs fabricated from GaAs/AlGaAs material systems have been reported by several researchers with peak detection wavelengths ranging from 15 μm to 26.9 μm [4,5,6,7,8,9]. Major effort on VLWIR QWIP development has been made at Jet Propulsion Laboratory (JPL) for space applications. A 128×128 pixel QWIP FPA with a 15 μm cutoff wavelength has been demonstrated by JPL with an NEDT of 30 mK at 45 K with 300 K background and $f/2.3$ optics [10]. This initial array gives excellent images with a 99.9 % operability and a 2.4 % uncorrected responsivity nonuniformity. Comparing the array results from both the MCT detector and GaAs QWIP at 15 μm , QWIP has higher operability and uniformity due to the mature GaAs MBE growth and processing technology.

The multi-color and broadband QWIP have also been widely investigated in recent years [1,11,12]. The multi-stack structure is usually employed to obtain multi-color detection in the MWIR and LWIR atmospheric spectral bands [11,12]. Voltage tunable QWIPs with asymmetrical double- or triple- coupled quantum well structures have also been reported for multi-color infrared detection by using the quantum confined Stark effect [13,14,15]. The broadband infrared detection has been achieved by using a wide variety of device structures with variable well width and barrier height in the quantum well [16,17,18,19]. Levine *et al.* have reported a voltage tunable LWIR QWIP using graded barrier quantum wells to achieve large shifts in the peak detection wavelength, spectral line-width, and cutoff wavelength [16]. Duboz *et al.* have studied the effect of asymmetrical barriers on the performance of GaAs/AlGaAs QWIPs [17]. In this paper we report two novel high performance InGaAs/AlGaAs/GaAs QWIPs using digital graded superlattice barriers (DGS LB) to achieve the linear- graded band gap (or linear graded composition) across the barrier region of the QWIP. The new structures enable

the broadband detection and significantly improve the responsivity under positive bias operation.

2. DESIGN CONSIDERATIONS OF VLWIR QWIPs

Several issues need to be considered when designing a VLWIR QWIP. In a VLWIR scenario, the temperature of the target is usually cold and the energy density of the blackbody radiation is small. This means that a higher response is needed from the detector. In order to tailor the peak detection wavelength of a QWIP to the VLWIR spectral region, the barrier height needs to be lowered and the well width needs to be increased with respect to MWIR (3-5 μm) and LWIR (8-12 μm) QWIPs. For QWIPs operating in the LWIR region, the typical well width is about 40 \AA to 45 \AA , and the aluminum mole fraction in the barrier is about 25% to 30%. While for VLWIR QWIPs, the well width is usually larger than 60 \AA , and the aluminum mole fraction in the barrier is less than 15% in order to achieve lower barrier energy and longer peak detection wavelength. The lower energy barrier and wider well width will result in a smaller activation energy, which means a higher thermionic emission of electrons from the quantum wells. In order to reduce the thermionic emission, which is the dominant mechanism of dark current in a VLWIR QWIP, the doping density in the well needs to be lower than that of a LWIR QWIP. In a LWIR QWIP, typical doping density is usually 0.5 to $1 \times 10^{18} \text{ cm}^{-3}$, whereas in a VLWIR QWIP the doping density is about 2 to $3 \times 10^{17} \text{ cm}^{-3}$. A balance between the responsivity and the dark current needs to be considered when choosing the doping density. The corresponding D^* will also be affected. In general, under the same operating temperature, the longer the detector cutoff wavelength, the smaller the D^* value. The electron density in the quantum well of a QWIP is usually very high, and hence the exchange energy plays an important role in the intersubband transition energy. This is especially true for a VLWIR QWIP in which the exchange energy greatly affects the detection peak wavelength due to the low barrier energy. We shall discuss each of these effects in detail next.

2.1 Blackbody Radiation

The blackbody radiation spectral density decreases very rapidly when the target

temperature decreases. Figure 1 shows the blackbody spectral density calculated under different temperatures using the blackbody spectral density formula

$$W(\lambda) = \frac{2\pi c^2 h}{\lambda^5} \frac{1}{\exp(hc/\lambda k_B T_B) - 1} \quad (1)$$

where c , h , k_B and T_B are the light speed in vacuum, Planck constant, Boltzmann constant, and the background temperature, respectively. As can be seen in Fig.1, when the target temperature changes from 300 K to 200 K, the peak wavelength will shift from 10 μm to 15 μm , and the spectral density will also decrease. For example, the maximum spectral density at 200 K is only 13% of the maximum density at 300 K. In order to efficiently detect the radiation from a target at 200 K, a 15 μm detector with higher responsivity, or lower dark current is highly desirable to maintain the same sensitivity as a 10 μm detector for a 300 K target.

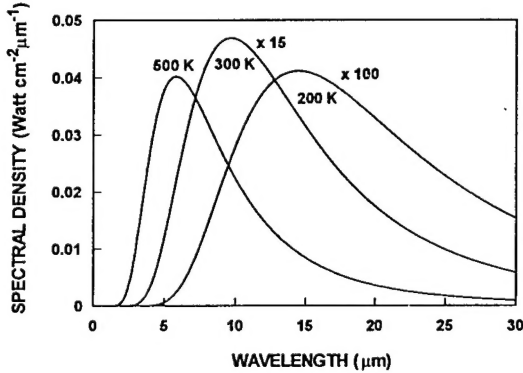


Figure 1. Blackbody spectral density at 200, 300, and 500 K.

2.2 Dark Current and Dynamic Resistance

The dark current I_d of a QWIP can be expressed as [20]

$$I_d = \frac{e m_w^* A}{\pi \eta^2 L_p} \frac{\mu F}{\sqrt{1 + (\mu F / v_s)^2}} \int_{E_i} f(E) T(E, F) dE \quad (2)$$

where e is the electronic charge, m_w^* is the electron effective mass in the well, A is the device area, L_p is the QWIP period length, μ is the electron mobility, F is the electric field inside the QWIP, v_s is the electron saturation velocity, $f(E)$ is the Fermi-Dirac distribution function, and $T(E, F)$ is the bias-dependent tunneling current transmission coefficient for a single barrier.

When the thermionic emission is dominant, the dark current can be expressed as

$$I_d = \frac{e^2 m_w^* A}{\pi \eta^2} \frac{\mu F^2}{\sqrt{1 + (\mu F / v_s)^2}} \frac{L_p}{L_w} \exp\left\{-\frac{(E_i - eF L_w - E_F - E_i)}{k_B T}\right\} \quad (3)$$

The dynamic impedance Z of a single period QWIP is defined as

$$Z = \frac{dV}{dI_d} \quad (4)$$

where V is the voltage drop across one period of the QWIP. In our calculations, the electron mobility and saturation velocity are taken as $2000 \text{ cm}^2 \text{ V}^{-1} \text{ s}^{-1}$ and $2 \times 10^6 \text{ cm/s}$, respectively. Figure 2 shows the calculated dark current versus bias for the 15.5 μm and 9.2 μm QWIPs at $T=40 \text{ K}$ and 60 K , respectively. The device structure for the 15.5 μm QWIP uses a 66 Å GaAs well and a 600 Å $\text{Al}_{0.15}\text{Ga}_{0.85}\text{As}$ barrier with a doping density of $2.5 \times 10^{17} \text{ cm}^{-3}$. The device structure for the 9.2 μm QWIP uses a 66 Å GaAs well with a doping density of $5 \times 10^{17} \text{ cm}^{-3}$ and a 600 Å $\text{Al}_{0.25}\text{Ga}_{0.75}\text{As}$ barrier. As can be seen from this figure, the dark current of the 9.2 μm QWIP is several orders of magnitude lower than that of the VLWIR QWIP under same bias and temperature condition. As a result, a large difference in the dynamic resistance of these two detectors is expected, as shown in figure 3. Therefore, in order for the 15.5 μm QWIP to have the same performance as the 9.2 μm QWIP, a lower operating temperature is required.

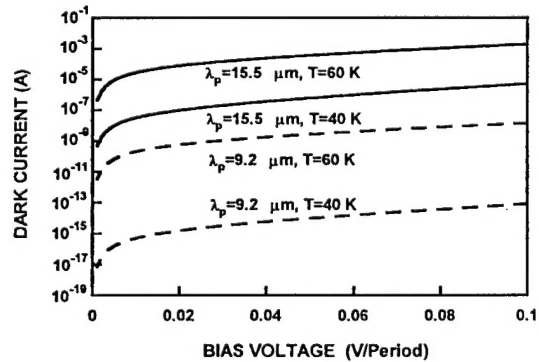


Figure 2. Calculated dark current versus bias for two QWIPs with peak wavelengths at 9.2 μm and 15.5 μm , respectively.

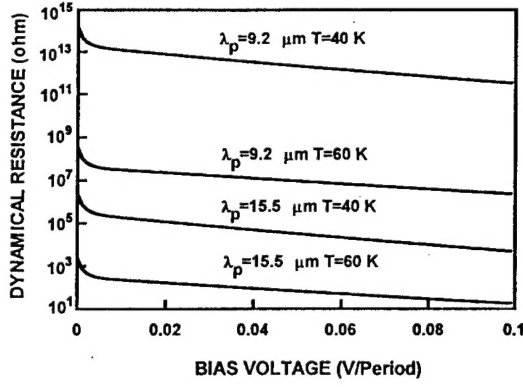


Figure 3. Calculated dynamic resistances for two QWIPs with peak wavelengths at 9.2 μm and 15.5 μm , respectively.

2.3 Detectivity

In a VLWIR QWIP the main dark current conduction mechanism is due to the thermionic emission across the barrier of quantum well. In general, over a wide range of temperatures and cutoff wavelengths, the detectivity can be expressed as [1]

$$D^* = D_0^* \exp(hc/2\lambda_c k T) \quad (5)$$

where λ_c is the cutoff wavelength.

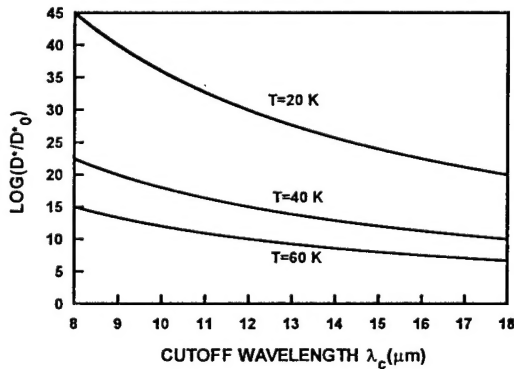


Figure 4. Variation of normalized detectivity with cutoff wavelength in the long and very long wavelength infrared (VLWIR) region.

As shown in figure 4, the detectivity decreases with increasing cutoff wavelength and temperature. This is due to the fact that with the increase of cutoff wavelength and temperature, the dark current and hence the dark current noise will increase significantly with increasing cutoff wavelength and temperature due to the nature of thermionic emission, while the responsivity

remains unchanged over a wide range of temperatures. Therefore, we come to the conclusion that in order to keep the same D^* when extending to longer wavelength, a lower operating temperature is needed.

2.4 Peak Wavelength Shift due to Exchange Interaction

When designing a QWIP, the energy states are obtained from the Schrödinger equation by taking into account the potential at the heterojunction caused by the energy band offset of the quantum well and barrier materials. The peak detection wavelength of a VLWIR QWIP can be calculated by using the transfer matrix method (TMM) [21]. West [22] has calculated the Coulomb interaction (repulsive) of the electrons in the quantum well and found that it is very small, which is canceled out with the dynamic electron plasma interaction. However, the experimental data he observed was about 6 meV higher than the calculated value for several QWIP structures. Taking into account the exchange interaction, excellent agreement between the theory and the experiment can be obtained [23]. For a VLWIR QWIP, the transition energy is relatively small and the influence of exchange energy becomes very significant. The exchange energy can be expressed as [23]

$$E_{\text{exch}} = -\frac{e^2}{2\epsilon} \int_0^{k_f} \frac{d^2 k'}{(2\pi)^2} \int dz \int dz' \frac{e^{-|k-k'|z}}{|k-k'|} |\phi_1(z)|^2 |\phi_1(z')|^2 \quad (6)$$

where $k_f = (2\pi\sigma)^{1/2}$, σ is the two-dimensional electron density in the quantum well, ϵ is the dielectric constant, k and k' are the in-plane wave vectors of electrons. Under normal doping condition, the exchange energy will lower the ground state subband energy by 5 to 10 meV and shifts the absorption peak to shorter wavelength.

As mentioned previously, in order to design a QWIP with peak detection wavelength in the VLWIR region, the barrier height should be lowered than that of the LWIR QWIP, and the well width should be increased with a lower doping density. As an example, let us consider the design of a VLWIR QWIP with a GaAs well width of L_w and doping density of $N_D = 2.5 \times 10^{17} \text{ cm}^{-3}$ and a 600 Å $\text{Al}_{0.15}\text{Ga}_{0.85}\text{As}$ barrier. Figure 5 shows the calculated variation of peak detection wavelength with well width L_w ; the dashed line is the result without considering the exchange

energy, while the solid line is the result of taking into account the exchange energy. The result agrees well with the experiment (e.g., at $L_w=66$ Å, the calculated peak wavelength is 15.54 μm and the measured value is 15.3 μm [4]). The reason for the transition peak wavelength to decrease with increasing well width is that: in this system the transition occurs between the bound state and the continuum state, and increasing well width has little effect on the excited continuum state energy but significantly decreases the bound state energy. As a result, the peak detection wavelength will decrease with the increase of well width and show a blue shift. As can be seen from this figure that the exchange energy plays an important role on the peak detection wavelength in a VLWIR QWIP. Therefore, special attention should be paid to the doping density while designing the VLWIR QWIP.

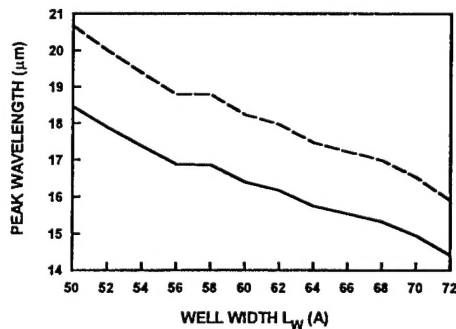


Figure 5 Variation of peak wavelength with well width in a GaAs/ $\text{Al}_{0.15}\text{Ga}_{0.85}\text{As}$ VLWIR QWIP. The dashed line is without considering the exchange energy, while the solid line is taking into account the exchange energy. L_w is the well width, and the barrier thickness is 600 Å.

3. VLWIR QWIP IN A MULTICOLOR QWIP STACK

As the infrared (IR) detector technology continues to advance, there is a growing demand for multi-color IR detectors for advanced sensing and imaging systems. IR detectors with more than two colors are highly desirable for temperature registration, chemical analysis, and target discrimination and identification. Using multiple stacks of QWIPs with intermediate contact layers, the capability of multicolor detection simultaneously, or sequentially by tuning the bias voltage has been demonstrated

[13,24]. When a VLWIR stack is incorporated in a multi-color QWIP, special attention has to be paid in the design. As can be seen from figure 3, the dynamic resistance of the $\lambda_p=15.5$ μm QWIP is much smaller than that of the $\lambda_p=9.2$ μm QWIP under the same bias condition. This means that the dark current, and hence the operating temperature of a multi-stack, multi-color QWIP will be limited by the longer wavelength QWIP stack. If operating temperature is the primary requirement, reducing the VLWIR dark current should be the main consideration when designing the detector. A low dynamic resistance also means a low voltage drop on this stack. When the multi-stack QWIP is used under voltage tunable mode, careful selection of period number, doping density and barrier width is necessary in order to realize the voltage tunability with a reasonable bias.

4. A 14.7 μm VLWIR QWIP

In this section we discuss the design, fabrication, characterization, and performance of a VLWIR QWIP. The QWIP structure is composed of 20 periods 80 Å $\text{In}_{0.04}\text{Ga}_{0.96}\text{As}$ well with doping density of $2 \times 10^{17} \text{ cm}^{-3}$ and a 500 Å $\text{Al}_{0.09}\text{Ga}_{0.91}\text{As}$ barrier. The schematic conduction band diagram of this QWIP is shown in figure 6. This structure is similar to those listed in table I with some unique features. First, a small amount of indium is added in the GaAs well region. This gives a smaller effective mass of electron, and therefore a higher absorption in the quantum well. Using aluminum free GaAs as a barrier has the advantage of having smaller defect center in the barrier which tends to reduce the dark current. However, electrons in the heavily doped GaAs contact layer can also tunnel into the quantum wells without any potential barrier, therefore causes an increase in dark current. In this design, a small amount of Al is added in the GaAs barrier to reduce the device dark current.

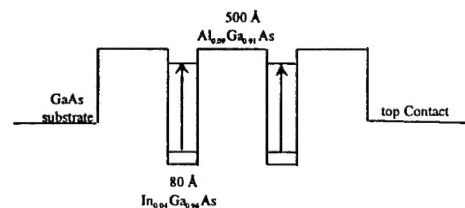


Figure 6. Schematic conduction band diagram of a 14.7 μm bound to bound state transition GaAs/AlGaAs QWIP.

The detector was designed with a peak wavelength at 14.5 μm . Theoretical calculation shows that the peak wavelength of this QWIP is at 16.1 μm without considering the exchange energy and 14.67 μm after taking into account the exchange energy. The detector is designed to use the bound to bound state intersubband transition for IR detection and for reducing the device dark current. Figure 7 shows the dark current density versus bias voltage with temperature as a parameter (40 to 60 K) for this device, along with the 300 K window current. The thermal activation energy due to thermionic emission can be determined from figure 7 using Arrhenius plot. Figure 8 shows the variation of activation energy with bias at 40 K. As can be seen from figure 8 that the activation energy versus bias voltage follows a straight line, as expected from Eq.(3). From this figure the thermal activation energy at zero bias was found to be 72.1 meV, in excellent agreement with the 75.5 meV calculated from the $E_b-E_1-E_F$. The spectral responsivity of this QWIP at 77 K under $\pm 2\text{V}$ is shown in figure 9. The responsivity peak was found to be at 14.7 μm , which is in excellent agreement with the calculated value when the exchange energy is taken into account. Figure 10 shows the variation of peak responsivity with bias at 40 K. As can be seen from this figure, the responsivity remains zero at very low bias voltages and increases rapidly for $|V_b| > 0.5\text{ V}$, which is the characteristics of the bound to bound state transition.

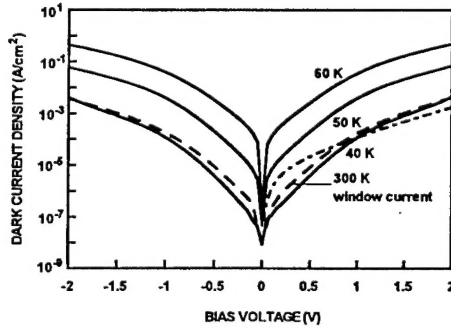


Figure 7. Measured dark current density versus bias voltage for the 14.7 μm VLWIR QWIP. The dash-dotted line is the calculated dark current density at 40 K obtained from Eq.(3).

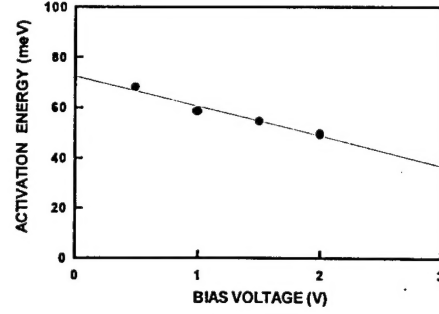


Figure 8. Activation energy versus bias voltage for the 14.7 μm VLWIR QWIP.

The detectivity can be expressed as

$$D_i^* = R_i \sqrt{\frac{A_d \Delta f}{4e I_d g}} \quad (7)$$

where R_i is the responsivity, A_d is the device area, Δf is the band width, e is the electron charge, I_d is the dark current, g is the noise gain. Noise can be obtained based on several assumptions: (i) the QWIP is considered as consisting of N statistically independent sections each made up of a barrier region with two doped quantum wells as contacts from which the carriers are emitted; (ii) the dominant dark current noise mechanism is generation-recombination (g-r) noise; (iii) the dominant dark current mechanism is thermionic emission; (iv) taking into account the image-force-induced barrier lowering. The noise gain can be obtained as [25]

$$g(V) = \frac{I_d R_0}{\frac{kT}{e} N^2 \exp\left(\frac{\Delta E}{kT}\right)} \quad (8)$$

where R_0 is the dynamic resistance at zero bias, N is the period number, k is the Boltzmann constant, ΔE is the barrier lowering, which is given by

$$\Delta E = e \sqrt{\frac{e V_b}{4 l_i \pi \epsilon_0 \epsilon_r}} \quad (9)$$

where V_b is the bias voltage across one period, l_i is one period length, ϵ_0 is the free space permittivity, and ϵ_r is the dielectric constant.

The D^* of this device was calculated at 40 K, 2 V bias using Eqs. (7) - (9) and the measured responsivity and device dark current. The result yields a D^* of $1.12 \times 10^{10} \text{ cm-Hz}^{1/2} \text{ W}^{-1}$. This D^* value is reasonably good for a VLWIR QWIP with cutoff wavelength at 16.3 μm . New VLWIR

QWIP structures are currently being studied to further improve the device performance.

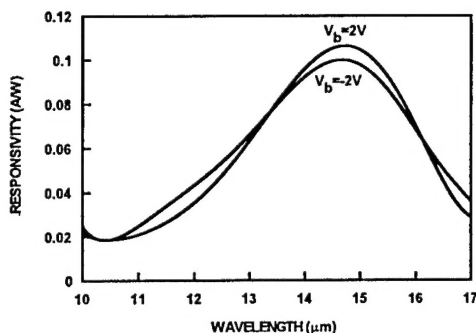


Figure 9. The spectral responsivity of the 14.7 μm VLWIR QWIP at $V_b = \pm 2\text{V}$ bias and 40K

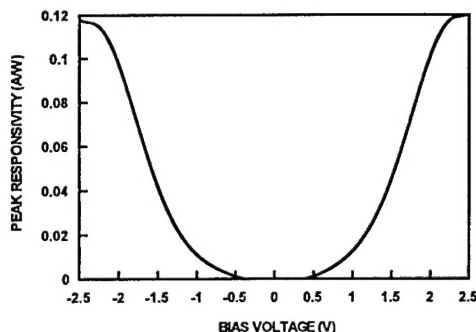


Figure 10. Variation of peak responsivity versus bias at 40 K for the 14.7 μm VLWIR QWIP.

5. DESIGN OF THE DIGITAL GRADED SUPERLATTICE BARRIERS QWIP

Two digital graded superlattice barriers QWIPs (DGSLB-QWIP) have been designed. The first QWIP structure (see Fig. 11) uses the InGaAs quantum well and digital graded GaAs/AlGaAs superlattice barriers to form the DGSLB-QWIP device. The second DGSLB-QWIP structure (Fig. 12) adds a thin undoped AlGaAs double barrier on both sides of the InGaAs quantum well for electron wave function confinement. The DGSLB structure was used to achieve the linear-graded barrier (i.e., linearly graded-band gap or graded composition barrier) in these devices. The standard MBE growth of the graded layer structure usually requires pausing the growth to change and stabilize the source temperature for the desired composition profile. As a result, it requires a longer growth time and may lead to more oxygen to be incorporated into the graded layer during the

growth interruption. The compositionally digital graded superlattice barriers (DGSLB) of the QWIP structures were grown using digital superlattices, which enable a stepwise linear composition grade to be formed without adjustment of the source temperature and the AlGaAs composition (i.e., using a fixed (15%) Al composition). The DGSLB structure can be obtained by using short-period superlattice structures with variable barrier/well thickness to change the Al mole fraction ratio and hence the energy band gap of the graded barrier. Adjusting the duty cycle can change the barrier/well thickness for each superlattice unit cell (5 periods, 2 nm thick). Therefore, using the DGSLB structure without changing the source temperature setting greatly simplifies the growth procedure and yields excellent wafer quality. The DGSLB layers were formed by using five superlattice unit cells in series in which the thin GaAs/Al_{0.15}Ga_{0.85}As layers with a 20 Å period were repeated 5 times for each superlattice unit cell. The device structure for the broadband (BB-) DGSLB-QWIP consists of a 50 Å In_{0.2}Ga_{0.8}As quantum well (Si doped to $7 \times 10^{17} \text{ cm}^{-3}$) and a 500 Å GaAs/Al_{0.15}Ga_{0.85}As DGSLB layer. Each superlattice unit cell in the DGSLB-layer has the combination of different barrier/well thicknesses (2.4/17.6, 4.8/15.2, 7.2/12.8, 9.6/10.4, and 12/8 Å) to obtain the target Al mole fractions of $x = 0.018, 0.036, 0.054, 0.072$, and 0.09 from the substrate side for the stepwise linear graded barrier layer. In the double barrier (DB-) DGSLB-QWIP, a thin (20 Å) undoped Al_{0.15}Ga_{0.85}As double barrier was grown between the DGSLB layers and the 88 Å In_{0.2}Ga_{0.8}As quantum well (Si doped to $7 \times 10^{17} \text{ cm}^{-3}$) to confine the electron wave functions and to create a resonant state (E_2) with the graded superlattice barrier. The DGSLB layer is composed of five 100 Å thick superlattice layer each with 5 periods of superlattices with (barrier/well) thicknesses of 1.6/18.4, 3.2/16.8, 4.8/15.2, 6.4/13.6, and 8/12 Å for the target Al mole fractions of $x = 0.012, 0.024, 0.036, 0.048$, and 0.06 in the Al_xGa_{1-x}As graded barrier layer. The 5000 Å contact layers (Si doped to $2 \times 10^{18} \text{ cm}^{-3}$) were grown at a substrate temperature of 600 °C, while the rest of the structure was grown at 510 °C to avoid indium (In) desorption from the InGaAs layers.

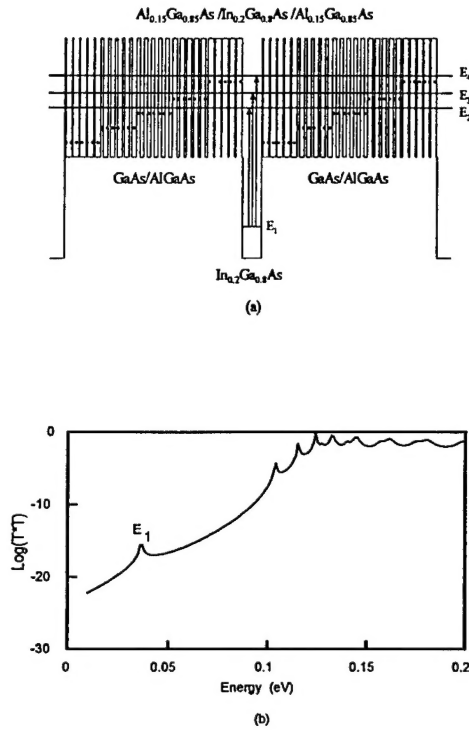


Figure 11 (a) The schematic conduction band diagram and (b) the calculated transmission coefficient versus energy at zero bias for the broadband (BB) DGS LB-QWIP.

Figure 11(a) and (b) show the schematic conduction-band diagram and the calculated transmission coefficient versus energy at zero bias using the multi-layer transfer matrix method (TMM) for the broadband (BB-) DGS LB-QWIP, respectively. The dotted lines denote the effective barrier height for each superlattice unit cell (5 periods, 20 Å/period) in the DGS LB. In this calculation, the strain effect due to lattice-mismatch between the InGaAs QW and the GaAs/AlGaAs barrier and the exchange energy due to the electron-electron interaction were considered. The E₁-E₂, E₁-E₃, and E₁-E₄ transitions contribute to the broadband detection under positive bias condition, while only transitions from the E₁ to E₄ states were observed under negative bias because the photo-generated carriers need to surmount the abrupt side of the barrier layers. Under positive bias condition, the effective barrier will decrease gradually with increasing bias to the lowest superlattice barrier height and then the bound states aligned by the DGS LB at zero bias will be the pseudo-continuum states over the DGS LB. Thus, the

broadband response can be achieved by the bound-to- pseudo-continuum (BTPC) state transitions under positive bias condition. On the contrary, the effective barrier height for the photo-excited electron transport will be at its maximum under negative bias condition and the slope of the DGS LB will be much steeper than under positive biases. Thus, the capture probability of the photo-excited electrons due to the bound-to-bound (BTB) transitions will be increased and normal spectral response is expected under negative bias condition.

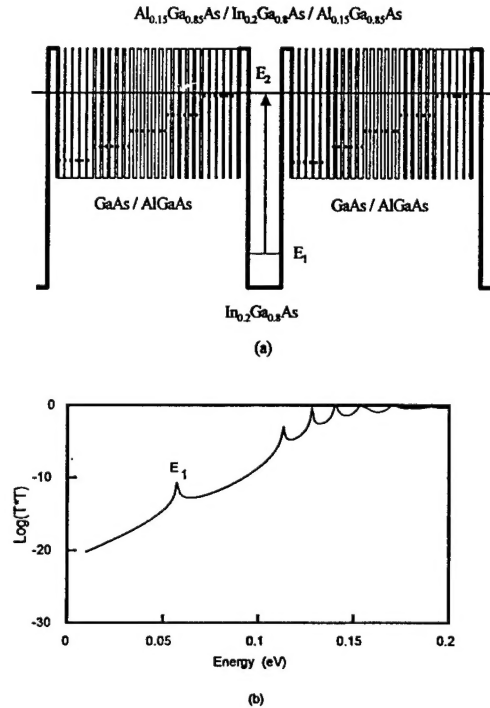


Figure 12 (a) The schematic conduction-band diagram and (b) the calculated transmission coefficient versus energy at zero bias for the double barrier (DB) DGS LB-QWIP.

Figure 12(a) and (b) show the schematic conduction-band diagram and the calculated transmission coefficient versus energy at zero bias for the double barrier (DB) DGS LB-QWIP device. The broadband response was not observed in this device because the wave function for the peak wavelength detection is strongly confined by the thin Al_{0.15}Ga_{0.85}As double-barrier and resonantly coupled to the wave functions of the E₂ state in the DGS LB region. Thus, normal spectral response with identical peak detection wavelength (at 12 μm) due to the E₁ to E₂ state transitions was obtained

under both negative and positive biases for this device.

7. MEASURED RESULTS OF THE DGSLB-QWIPs

We have performed the dark current-voltage (I-V) and spectral response measurements on both DGSLB-QWIPs under negative and positive bias conditions. Excellent results were obtained in the photoresponse measurements on these devices. A very broadband photo-response ($\lambda_p = 7 \sim 16 \mu\text{m}$) under positive bias condition and a normal spectral response with voltage tunable peak wavelength under negative bias condition were obtained for the BB- DGSLB-QWIP device. Normal spectral response was observed in the DB- DGSLB-QWIP with peak detection wavelength at $12 \mu\text{m}$. Due to the asymmetrical graded barrier structure, a very large responsivity ($R_i = 3 \text{ A/W}$ at $12 \mu\text{m}$, 1V and 35K) was obtained in this device under positive bias condition. Results of the dark current and spectral photoresponse measurements on both devices are discussed next.

7.1 Dark I-V Characteristics

Figure 13(a) and (b) show the dark current density as a function of applied bias voltage for the BB- and DB- DGSLB QWIPs measured at different temperatures ($T = 35, 50, 60,$ and 77K), respectively. The 300K background window currents with a field of view (FOV) of 180° were also given in Fig. 13(a) and 13(b).

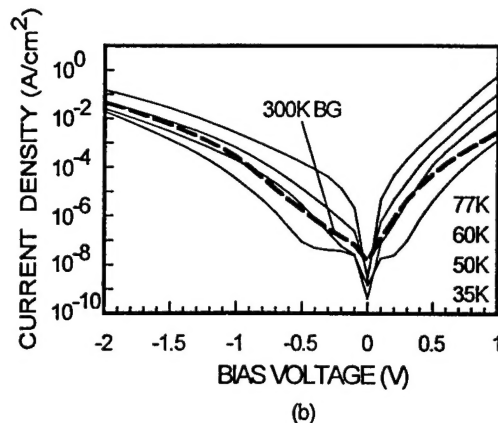
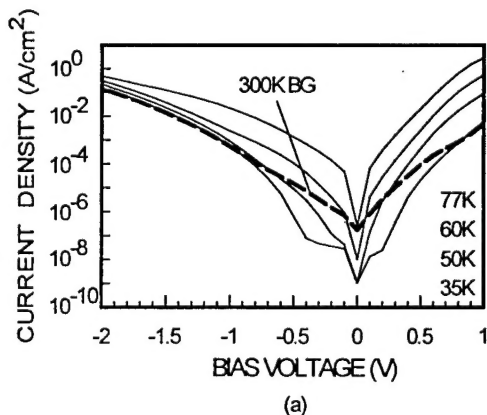


Figure 13 The dark current density versus bias voltage for (a) the BB- DGSLB QWIP and (b) the DB- DGSLB QWIP. The dashed line is the 300 K background photocurrent.

As expected in the asymmetrical quantum well structure, the dark currents and photoresponse are also highly asymmetrical under positive and negative bias conditions, which is attributed to the different effective barrier profiles under negative and positive biases, as explained previously. In both devices we have observed a much higher dark current and photo-response under positive bias condition. This is due to the barrier lowering of the DGSLB and the electron launching under positive bias condition. The BB- DGSLB QWIP device is under background limited performance (BLIP) between -1V and $+0.75\text{V}$ at $T = 35\text{K}$ and the BLIP temperature was 55K while the DB- DGSLB-QWIP is under BLIP between -2V and $+0.35\text{V}$ at $T = 50\text{K}$.

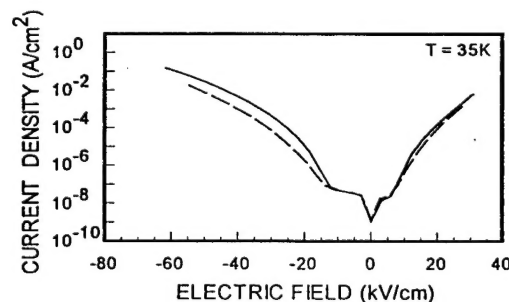


Figure 14 A comparison of the dark current density versus the electric field for the BB- DGSLB-QWIP (solid line) and the DB- DGSLB QWIP (dashed line).

Figure 14 shows a comparison of the dark current density as a function of the electric field at $T = 35\text{K}$ for these two QWIP devices. Although the DB- DGSQB-QWIP exhibits a longer peak wavelength ($12\text{ }\mu\text{m}$ peak) than the BB- DGSQB-QWIP ($11\text{ }\mu\text{m}$ peak) under negative biases, the dark current density of the DB- DGSQB-QWIP is slightly lower than that of the BB- DGSQB-QWIP due to the use of a thin undoped $\text{Al}_{0.15}\text{Ga}_{0.85}\text{As}$ double-barrier around the InGaAs quantum well which tends to reduce the carrier transport probability under dark condition.

7.2 Spectral Responsivity and Detectivity

The spectral response was measured at $T = 35\text{K}$ for both DGSQB-QWIPs by using a $1/8$ monochromator, a calibrated blackbody IR source ($T = 1273\text{K}$), and a closed cycle liquid helium cryostat at 200 Hz chopped frequency. The spectral responsivity can be calculated by

$$R_s = \frac{I_p}{P_{in}}, \quad (10)$$

where I_p is the photocurrent output (A), and P_{in} is the input IR radiation power (W), which can be expressed as

$$I_p = \frac{V_p}{R_f}, \quad (11)$$

$$P_{in} = A_d H_{in}, \quad (12)$$

where V_p is the photovoltage of the photodetector, R_f is the gain of the transimpedance amplifier (TIA), A_d is the photodetector area (cm^2), and H_{in} is the input irradiance (W/cm^2), which is given by

$$H_{in} = \frac{V_{pyro} T_w T_d}{R_p A_p}, \quad (13)$$

where V_{pyro} is the photovoltage of the pyroelectric detector, T_w is the transmissivity of the entrance window of the cryogenic system, T_d is the transmissivity of the photodetector, R_p is the responsivity of the pyroelectric detector (V/W), and A_p is the active area of the pyroelectric detector (cm^2), respectively. The pyroelectric detector is used to calibrate the input power of the infrared radiation from the blackbody IR source onto the photodetector.

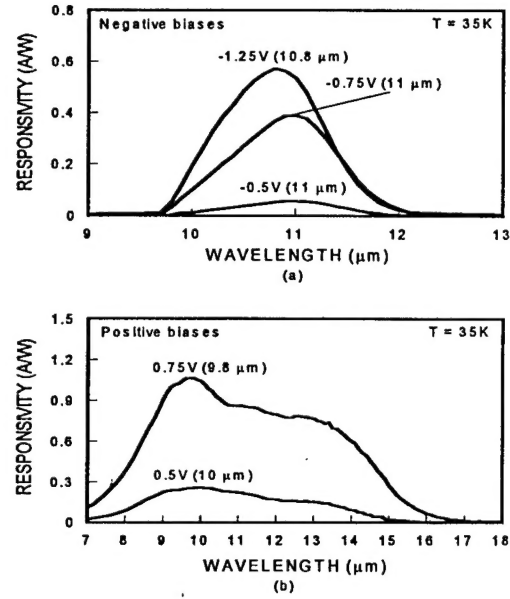


Figure 15 The spectral responsivity of the BB-DGSQB QWIP device at $T = 35\text{K}$: (a) at negative bias and (b) at positive bias condition.

Figure 15(a) and (b) show the spectral responsivity of the BB- DGSQB-QWIP at $T = 35\text{K}$ under (a) negative and (b) positive bias conditions. The peak wavelength was blue-shifted from $11\text{ }\mu\text{m}$ to $10.8\text{ }\mu\text{m}$ between -0.75V and -1.25V under negative bias condition. The absolute responsivity increases with the applied bias due to the increase in photoconductive gain with increasing bias. The peak responsivities at $\lambda_p = 10.8\text{ }\mu\text{m}$ and $9.8\text{ }\mu\text{m}$ were found to be 0.57 A/W and 1.07 A/W at $V_b = -1.25\text{V}$ and $+0.75\text{V}$, respectively. It is noted that a very broad spectral bandwidth was obtained under positive bias condition in this device. The full-width half-maximum (FWHM) spectral bandwidth of this device at $V_b = -1.25\text{V}$ was found to be $\Delta\lambda/\lambda_p = 13\%$ while FWHM spectral bandwidths at $V_b = +0.75\text{V}$ and $+0.5\text{V}$ were found to be $\Delta\lambda/\lambda_p = 62\%$ and 54% , respectively. This broadband detection feature was attributed to the formation of pseudo- continuum states by the overlapping of E_2 , E_3 , and E_4 wave functions, which enables the broadband detection from the E_1 to the E_2 , E_3 , and E_4 states under positive bias condition.

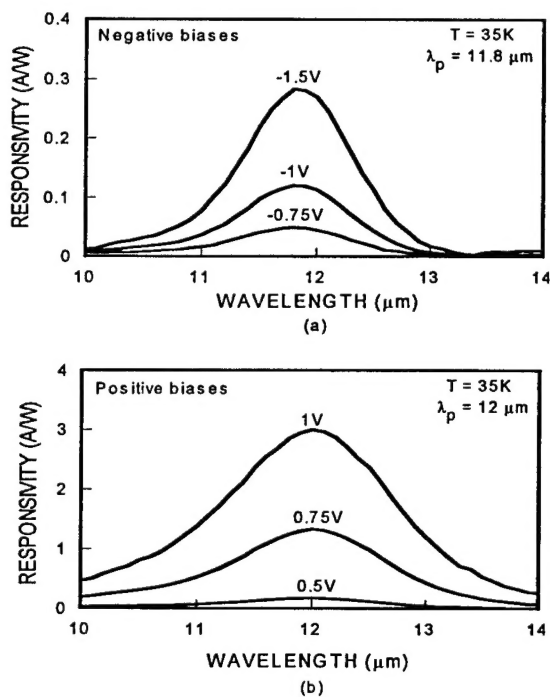


Figure 16 The spectral responsivity of the DB-DGSLB QWIP at $T = 35\text{K}$: (a) at negative and (b) at positive bias condition.

Figure 16(a) and (b) show the spectral responsivity of the DB-DGSLB-QWIP at $T = 35\text{K}$ under (a) negative and (b) positive bias conditions. The maximum peak responsivity at $\lambda_p = 11.8\text{ }\mu\text{m}$ was found to be 0.28 A/W at $V_b = -1.5\text{V}$ and $T = 35\text{K}$. However, the spectral responsivity was dramatically increased under positive bias condition due to the graded barrier lowering and electron launching effect. The peak responsivity at $V_b = +1\text{V}$ was 3 A/W at $\lambda_p = 12\text{ }\mu\text{m}$ and $T = 35\text{K}$. The FWHM spectral bandwidth at $V_b = -1.5\text{V}$ and $+1\text{V}$ were $\Delta\lambda/\lambda_p = 11\%$ and 17% , respectively. A slightly broader spectral bandwidth detection was obtained under positive bias condition. The peak detection wavelength for this device was attributed to the E_1 - E_2 state transitions.

The detectivity of both QWIPs was calculated from the results of the responsivity and dark current measurements by using Eqs (7)-(9). In the first DGSLB-QWIP, the detectivity at $V_b = -0.75\text{V}$ and 0.75V were found to be $6.71 \times 10^{10}\text{ cm Hz}^{1/2}/\text{W}$ at $\lambda_p = 11\text{ }\mu\text{m}$ and $1.89 \times 10^{10}\text{ cm Hz}^{1/2}/\text{W}$ at $\lambda_p = 9.8\text{ }\mu\text{m}$, respectively. The detectivity at $V_b = -1.5\text{V}$ and $+1\text{V}$ for the DB DGSLB-QWIP were found to be $4.79 \times 10^9\text{ cm}$

$\text{Hz}^{1/2}/\text{W}$ at $\lambda_p = 11.8\text{ }\mu\text{m}$ and $2.54 \times 10^{10}\text{ cm Hz}^{1/2}/\text{W}$ at $\lambda_p = 12\text{ }\mu\text{m}$, respectively.

The following table lists some performance parameters of the devices mentioned in this paper. In the table T is the device temperature at which measurement is performed, λ_c is the cutoff wavelength and D^* is the detectivity.

Table 1 Performance parameters of some devices.

device	T (K)	λ_c (μm)	D^* ($\text{cmHz}^{1/2}\text{W}^{-1}$)
D-1	40	16.3	1.12×10^{10}
D-2	35	14.3	1.89×10^{10}
D-3	35	12.9	2.54×10^{10}
JPL	55	14.9	1.6×10^{10}

D-1: the device with peak wavelength at $14.7\text{ }\mu\text{m}$.

D-2: broadband DGSLB QWIP

D-3: double barrier DGSLB QWIP

JPL: JPL FPA discussed in reference 10.

8. SUMMARY

In summary, the latest development in VLWIR QWIPs has been reviewed and fundamental device physics and design considerations on VLWIR discussed. We also demonstrated three QWIP structures with one in LWIR, one in VLWIR, and one broad band. The devices show promising performance and improvements are under way to meet system requirements.

ACKNOWLEDGEMENT

This work was partially supported by BMDO/TO (ARL) and by US Army Research Office (UF) under grant no. DAAG55-98-1-0325.

REFERENCES

1. B.F. Levine, J. Appl. Phys., **74**, R1, (1993).
2. S.D. Gunapala and K.M.S.V. Bandara, Thin Films, **21**, 113 (1995).
3. Sheng S. Li, Journal of the Chinese Institute of Electrical Engineering, **2**, 37 (1995).
4. G. Sarusi, S.D. Gunapala, J.S. Park and B.F. Levine, J. Appl. Phys., **76**, 6001 (1994).
5. B.F. Levine, A. Zussman, J.M. Kuo and J. De Jong, J. Appl. Phys., **71**, 5130 (1992).

6. S.D. Gunapala, K.M.S.V. Bandara, B.F. Levine, G. Sarusi, D.L. Sivco and A.Y. Cho, *Appl. Phys. Lett.*, **64**, 2288 (1994).
7. C.Y. Lee, M.Z. Tidrow, K.K. Choi, W.H. Chang, L.F. Eastman, F.J. Towner and J.S. Ahearn, *J. Appl. Phys.*, **75**, 4731 (1994).
8. A.G.U. Perera, W.Z. Shen, S.G. Matsik, H.C. Liu, M. Buchanan and W.J. Schaff, *Appl. Phys. Lett.*, **72**, 1596 (1998).
9. J. Chu, Sheng S. Li, A. Singh and P. Ho, *Appl. Phys. Lett.*, **72**, 1664 (1998).
10. S. D. Gunapala, J. S. Park, G. Sarusi, T. L. Lin, J. K. Liu, P. D. Maker, R. E. A. Muller, C. A. Shott, and T. Hoelter, *IEEE Trans. Electron. Devices* **44**, 45 (1997).
11. J. C. Chiang, Sheng S. Li, and A. Singh, *Appl. Phys. Lett.*, **71**, 3546 (1996).
12. M. Z. Tidrow, Xudong Jiang, Sheng S. Li, and K. Bacher, *Appl. Phys. Lett.*, **74**, 1335 (1999).
13. Jung-Chi Chiang, Sheng S. Li, M. Z. Tidrow, P. Ho, M. Tsai, and C. P. Lee, *Appl. Phys. Lett.*, **69**, 2412 (1996).
14. H. Schneider, K. Kheng, M. Ramsteiner, J. D. Ralston, F. Fuchs, and P. Koidl, *Appl. Phys. Lett.*, **60**, 1471 (1992).
15. A. Brandel, A. Fraenkel, E. Finkman, G. Bahir, G. Livescu, and M. T. Asom, *Semicond. Sci. Technol.*, **8**, S412 (1993).
16. B. F. Levine, C. G. Bethea, V. O. Shen, and R. J. Malik, *Appl. Phys. Lett.*, **57**, 383 (1990).
17. J. Y. Duboz, L. Saminadayar, and J. M. Gerard, *J. Appl. Phys.*, **78**, 2803 (1995).
18. S. V. Bandara, S. D. Gunapala, J. K. Liu, E. M. Luong, J. M. Mumolo, W. Hong, D. K. Sengupta, and M. J. Mckelvey, *Appl. Phys. Lett.*, **72**, 2427 (1998).
19. Sheng S. Li, J. Chu, J. C. Chiang, J. H. Lee, and A. Singh, *Proc. of SPIE* **3629**, 138 (1999).
20. B.F. Levine, C.G. Bethea, G. Hasnain, V.O. Shen, E. Pelve, R.R. Abbott and S.J. Hsieh, *Appl. Phys. Lett.*, **56**, 851 (1990).
21. M.O. Vassell, Johnson Lee and H.F. Lockwood, *J. Appl. Phys.*, **54**, 5206 (1983).
22. Lawrence West, "Spectroscopy of GaAs Quantum Wells", Ph. D. Thesis, July 1985.
23. K.M.S.V. Bandara, D.D. Coon, Byungsung O, Y.F. Lin and M.H. Francombe, *Appl. Phys. Lett.*, **53**, 1931 (1988).
24. M.Z. Tidrow, J.C. Chiang, Sheng S. Li and K.Bacher, *Appl. Phys. Lett.*, **70**, 859 (1997).
25. Daniel C. Wang, Ph.D Thesis, University of Florida (1996).